crystals

MDPI

Article

The Complete Series of Lanthanoid-Chloranilato Lattices with Dimethylsulfoxide: Role of the Lanthanoid Size on the Coordination Number and Crystal Structure

Samia Benmansour *, Carlos J. Gómez-García * and Antonio Hernández-Paredes

Departamento de Química Inorgánica, Universidad de Valencia, C/Dr. Moliner 50, Burjasot, 46100 Valencia, Spain; antonio.hernandez-paredes@uv.es

* Correspondence: sam.ben@uv.es (S.B.); carlos.gomez@uv.es (C.J.G.-G.)

Abstract: We report the synthesis, structural and magnetic characterization of the complete series of lanthanoid-based chloranilato 2D lattices with dimethylsulfoxide (dmso) formulated as: $[Ln_2(C_6O_4Cl_2)_3(dmso)_6]$ with Ln = La(**1**), Ce(**2**), Pr(**3**), Nd(**4**), Sm(**5**), Eu(**6**), Gd(**7**) and Tb(**8**) or $[Ln_2(C_6O_4Cl_2)_3(dmso)_4]\cdot 2dmso\cdot 2H_2O$ with Ln = Dy(**9**), Ho(**10**), Er(**11**), Tm(**12**) and Yb(**13**); $C_6O_4Cl_2^{2-}$ = dianion of 3,6-dichloro-2,5-dihydroxy-1,4-benzoquinone = chloranilato. Single crystal X-ray analysis shows that the largest Ln(III) ions (La–Tb, **1**–**8**) crystallise in the monoclinic $P2_1/n$ space group (phase I), whereas the smallest ones (Dy–Yb, **9**–**13**) crystallise in the triclinic P-1 space group (phase II). Both phases show a (6,3)-2D network with the typical hexagonal honeycomb lattice, although phase I presents important distortions, resulting in rectangular cavities with a brick-wall orientation. The largest ions (phase I) show a coordination number of nine with a capped square antiprismatic geometry in contrast to the smallest ions (phase II) that present a coordination number of eight with a triangular dodecahedral geometry. Magnetic measurements show that all the Ln(III) ions are magnetically well isolated, leading to the presence of a field induced single-ion magnet behaviour in the Er derivative, with an energy barrier of 23(2) K for DC fields of 20, 50 and 100 mT.

Keywords: chloranilato; lanthanoids; 2D lattices; honeycomb lattice; dmso; crystal structures; 6,3-networks; slow relaxation of the magnetization; field-induced single-ion magnet

check for updates

Citation: Benmansour, S.; Gómez-García, C.J.; Hernández-Paredes, A. The Complete Series of Lanthanoid-Chloranilato Lattices with Dimethylsulfoxide: Role of the Lanthanoid Size on the Coordination Number and Crystal Structure. *Crystals* **2022**, *12*, 261. https://doi.org/10.3390/cryst12020261

Academic Editor: Stefano Carli

Received: 2 February 2022
Accepted: 11 February 2022
Published: 15 February 2022

Publisher's Note: MDPI stays neutral with regard to jurisdictional claims in published maps and institutional affiliations.

Copyright: © 2022 by the authors. Licensee MDPI, Basel, Switzerland. This article is an open access article distributed under the terms and conditions of the Creative Commons Attribution (CC BY) license (https://creativecommons.org/licenses/by/4.0/).

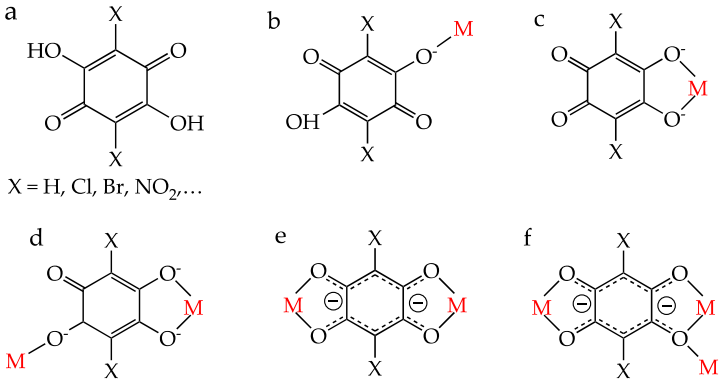
1. Introduction

Metal-organic frameworks (MOFs) are, according to IUPAC [1], coordination networks with organic ligands containing potential voids. The interest in these porous materials has experienced an exponential increase in the last two decades that has led to the synthesis of thousands of MOFs with large surface areas and porosity, chemically functionalized cavities and flexible skeletons [2]. One of the key issues to design MOFs with tailored properties is to control and modulate the shape and size of the cavities [3,4], as this control may lead to interesting applications in fields such as catalysis [5], gas storage and separation [6], water absorption [7], optical, magnetic and chemical sensing [8–10], electrical [11] and proton conductivity [12], ferroelectricity [13] or magnetism [14], among others. They may even show a combination of several properties [15].

Although most MOFs are three-dimensional (3D) lattices, there is an increasing interest in two-dimensional (2D) MOFs, boosted by the discovery of graphene-like 2D materials. This interest has led to the synthesis of several 2D MOFs with interesting properties and applications [16,17].

The use of anilato-type ligands (3,6-disubstituted-2,5-dihydroxy-1,4-benzoquinone dianion = $C_6O_4X_2^{2-}$, Scheme 1a) to prepare MOFs constitutes a very appealing strategy since these ligands may present several different coordination modes, including monodentate (*1kO*, Scheme 1b), bidentate ($1k^2O,O'$, Scheme 1c), monodentate-bidentate ($1kO;2k^2O',O''$, Scheme 1d), bis-bidentate ($1k^2O,O';2k^2O'',O'''$, Scheme 1e) and more complex modes

($1k^2O,O';2k^2O'',O''';3kO''$, Scheme 1f) [18], giving rise to many different structural types. In fact, anilato is topologically equivalent to oxalate ($C_2O_4^{2-}$), bearing the same anionic charge and, accordingly, forms very similar structures as discrete tris(anilato)metalate complexes [19,20] and extended one-, two- and three-dimensional lattices, although with larger channels and cavities [18,21–25].



Scheme 1. (**a**) Anilato ligands. (**b**–**f**) Different coordination modes of anilato ligands.

From the magnetic point of view, anilato ligands mediate weak antiferromagnetic couplings, modulated by X, when connecting transition metals [26,27], but they show a negligible coupling when connecting lanthanoids, due to the poor overlap of Ln(4f) and O(2d) orbitals [28–33]. This isolation has resulted in the observation of single-ion magnet behaviour in a few examples of Ln-anilato lattices [34–37].

The different structures, topologies and properties, including magnetic, optical, electrochemical, gas/solvent sorption/exchange and processing as thin films of all the known lanthanoid-anilato complexes and lattices have been revised very recently by some of us [25]. The synthesis of lanthanoids with anilato ligands shows that there are four factors influencing the final structure and topology: (i) the X groups in the anilato ligands, (ii) the size of the Ln(III) ion, (iii) the size and shape of the solvent molecules acting as co-ligands and (iv) the synthetic method [25]. These factors play a key role in determining the structure of these lattices because in most Ln-anilato coordination polymers, the Ln(III) ions are coordinated by three bidentate anilato ligands and complete their octa- or nona-coordination [25,29,32,38] with two or three solvent molecules with a high coordination capacity towards Ln(III) ions as water, dmso, dimethylformamide (dmf), dimethylacetamide (dma) or formamide (fma) [39,40].

Here, we analyse in detail the role of the size of the Ln(III) ion on the final structure of the complete series prepared with chloranilato $(C_6O_4Cl_2)^{2-}$ and dimethylsulfoxide (dmso) as solvent. Thus, we have prepared single crystals and solved all the X-ray crystal structures of the complete series obtained combining Ln(III), $C_6O_4Cl_2^{2-}$ and dmso. This series can be formulated as $[Ln_2(C_6O_4Cl_2)_3(dmso)_6]$ with Ln = La(**1**), Ce(**2**), Pr(**3**), Nd(**4**), Sm(**5**), Eu(**6**), Gd(**7**) and Tb(**8**) or $[Ln_2(C_6O_4Cl_2)_3(dmso)_4]\cdot 2dmso\cdot 2H_2O$ with Ln = Dy(**9**), Ho(**10**), Er(**11**), Tm(**12**) and Yb(**13**). As we will see below, the large ions (La–Tb, **1**–**8**) crystallise in the monoclinic $P2_1/n$ space group (phase I), while the small ones (Dy–Yb, **9**–**13**) crystallise in the triclinic *P*-1 space group (phase II). Both phases show (6,3)-2D networks although with important differences as a consequence of the different sizes of the Ln(III) ions. We present here a comparative structural study of all the compounds in this series. Since the structure of the Er(**11**) and Dy(**9**) derivatives have been recently reported by us [32,37], we only include them here for comparative purposes.

We also present the magnetic properties of all the members of the series and show that the Er derivative (**11**) displays a field-induced single-ion magnet behaviour with an activation energy of 23(2) K. Note that the magnetic properties of the Er and Dy derivatives have also been recently reported by us [32,37], although the field-induced single ion magnet behaviour of the Er derivative was not reported.

2. Materials and Methods

Chloranilic acid, the Ln(III) nitrates and dmso are all commercial and were used as received without any further purification. All the salts were obtained as single crystals using the same method as described for the La(III) derivative (see below). The exact amounts and precursor salts used for each compound and the aspect of the compounds are listed in Table S1.

Synthesis of $[La_2(C_6O_4Cl_2)_3(dmso)_6]$ (1) Single crystals of compound **1** were obtained by carefully layering, at room temperature, a solution of chloranilic acid, $H_2C_6O_4Cl_2$, (4.2 mg, 0.02 mmol) in 5 mL of methanol on top of a solution of $La(NO_3)_3.6H_2O$ (8.8 mg, 0.02 mmol) in 5 mL of dmso. The tube was sealed and allowed to stand for five weeks to obtain thin block-shaped violet single crystals suitable for X-ray diffraction that were freshly picked and covered with paratone oil in order to avoid solvent loss to be characterized by single crystal X-ray diffraction. Compounds **2–13** were prepared following the same method but changing the Ln(III) nitrate (see Table S1, supporting information).

Magnetic measurements. Magnetic susceptibility measurements were carried out in the temperature range of 2–300 K with an applied magnetic field of 0.1 T, on polycrystalline samples of compounds **1**–**13** (freshly prepared to avoid solvent loss), with a Quantum Design MPMS-XL-5 SQUID susceptometer. AC measurements were performed on a sample of compound **11** (with a mass of 11.863 mg) in the temperature range of 1.9–5.0 K with different applied dc fields (in the range 0–500 mT) with an AC field of 8 Oe oscillating in the range of 10–10,000 Hz, using a Quantum Design PPMS-9 instrument. The susceptibility data were corrected for the sample holder previously measured using the same conditions and for the diamagnetic contribution of the samples as deduced by using Pascal's constant tables [41].

X-ray crystallography. Single crystals of compounds **1**–**13** were mounted on glass fibres using a viscous hydrocarbon oil to coat the crystal and then transferred directly to the cold nitrogen stream for data collection. X-ray data were collected at 120 K on a Supernova diffractometer equipped with a graphite monochromated Enhance (Mo) X-ray Source (λ = 0.71073 Å). The program CrysAlisPro, Oxford Diffraction Ltd., was used for unit cell determinations and data reduction [42]. Empirical absorption correction was performed using spherical harmonics, implemented in the SCALE3 ABSPACK scaling algorithm. Compounds **1**–**8** crystallize in the monoclinic $P2_1/n$ space group whereas compounds **9**–**13** crystallize in the triclinic P-1 space group. The origin of this difference will be discussed in the structural description section. Crystal structures were solved via direct methods with the SIR92 program [43], and refined against all F^2 values with the SHELXL-2014 program [44], using the WinGX2014.1 graphical user interface [45]. Non-hydrogen atoms were refined anisotropically (when no disorder was present) and hydrogen atoms were assigned fixed isotropic displacement parameters. Hydrogen atom positions were calculated geometrically and refined using the riding model. A summary of the data collection and structure refinements for compounds **1**–**13** is given in Tables S2–S6 (see supporting information). Crystallographic data for the structures reported in this paper have been deposited in the Cambridge Crystallographic Data Center under reference numbers CCDC 2142143-2142153. These data can be downloaded via www.ccdc.cam.ac.uk/deposit@ccdc.cam.ac.uk (accessed on 10 February 2022).

3. Results

3.1. Synthesis

The use of different $Ln(NO_3)_3{\cdot}nH_2O$ with chloranilic acid and dmso with the same synthetic conditions leads to two different structural types, depending on the size of the lanthanoid ion. Thus, the eight largest ions (La–Tb) crystallize in the series (Phase I) formulated as $[Ln_2(C_6O_4Cl_2)_3(dmso)_6]$ with Ln = La(**1**), Ce(**2**), Pr(**3**), Nd(**4**), Sm(**5**), Eu(**6**), Gd(**7**) and Tb(**8**), whereas the smallest ions (Dy–Yb) crystallize in a different series (Phase II) formulated as $[Ln_2(C_6O_4Cl_2)_3(dmso)_4]{\cdot}2dmso{\cdot}2H_2O$ with Ln = Dy(**9**), Ho(**10**), Er(**11**), Tm(**12**) and Yb(**13**). Since the structure of phase II has recently been reported by us in

compounds **9** and **11**, we will only describe in detail the structure of phase I and compare it with the phase II structure.

*3.2. Crystal Structure of $[Ln_2(C_6O_4Cl_2)_3(dmso)_6]$ with Ln = La(**1**), Ce(**2**), Pr(**3**), Nd(**4**), Sm(**5**), Eu(**6**), Gd(**7**) and Tb(**8**)*

Compounds **1**–**8** are isostructural and, therefore, only the structure of compound **4** will be described in detail. A comparative study of compounds **1**–**8** with those of phase II (**9**–**13**) is performed below.

Compounds **1**–**8** crystallize in the monoclinic $P2_1/n$ space group. The asymmetric unit (Figure 1) contains one Ln ion, one and a half chloranilato ligands and three coordinated dmso molecules (with a positional disorder of the S and one methyl group in one or two of the dmso coordinated molecules). The general formula is, therefore, $[Ln_2(C_6O_4Cl_2)_3(dmso)_6]$ with Ln = La(**1**), Ce(**2**), Pr(**3**), Nd(**4**), Sm(**5**), Eu(**6**), Gd(**7**) and Tb(**8**).

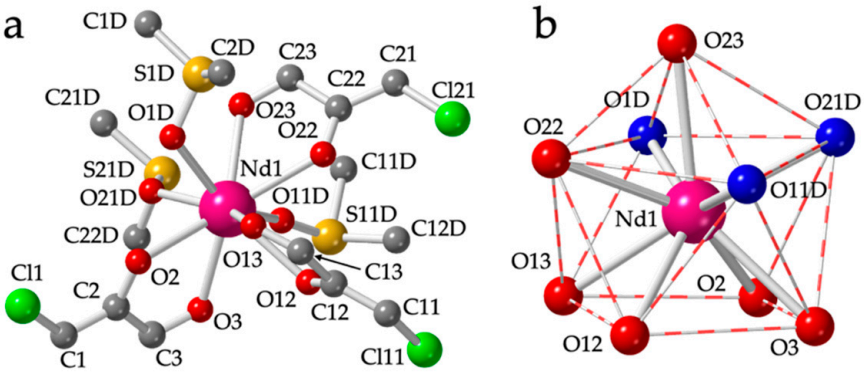


Figure 1. (**a**) Asymmetric unit of compound **4** showing the labelling scheme. Only one of the two possible positions of the S atom of one of the coordinated dmso molecules is shown for clarity. H atoms are omitted for clarity. (**b**) Coordination environment of Nd atom in compound **4** (the O atoms of the dmso molecules are depicted in blue).

The Ln(III) ion is surrounded by nine O atoms, from three chelating chloranilato ligands (O2, O3, O12, O13, O22 and O23) and from three dmso molecules (O1D, O11D and O21D). The continuous SHAPE analysis shows that the coordination geometry corresponds to distorted capped square antiprism (CSAPR-9) geometry (Table S7, supporting information) [46]. The three O atoms of the dmso molecules are located in the upper capped square face of the capped square antiprism (with a so-called *030* disposition). Note that the location of the O atoms of the solvent molecules (and of the three chelating anilato ligands) is a key point to determine the final structure and the distortions of the hexagonal cavities.

The average Ln–$O_{anilato}$ bond distances are longer than the Ln–O_{dmso} ones due to the formation of the five-membered chelate ring (see below). As expected, there is a continuous decrease of the Ln–O bond distances along the lanthanoids series with an abrupt change between the Tb and Dy derivatives, due to the change of coordination number, geometry and phase (see below).

Compounds **1**–**8** show a layered structure, with neutral layers formulated as $[Ln_2(C_6O_4Cl_2)_3(dmso)_6]$. The layers are very corrugated (Figure 2a) and are packed parallel to the (101) direction in an eclipsed way, giving rise to channels perpendicular to the layers (Figure 2b).

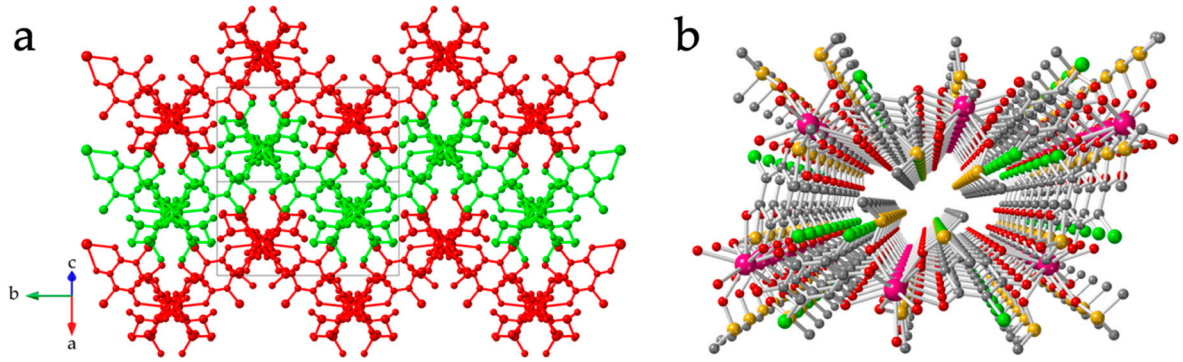


Figure 2. (**a**) View of three consecutive corrugated layers in compound **4**. (**b**) Perspective view of one channel along the direction perpendicular to the layers.

The layers show a honeycomb network with very distorted hexagonal (6,3)-gon topology where each Ln(III) ion in connected to other three Ln(III) ions through three bis-bidentate chloranilato bridges, generating six membered, very deformed, hexagonal rings that appear as rectangles when viewed down the *a* direction (Figure 3a). The Ln(III) ions are located in the vertex and in the centre of the long side of these rectangular cavities. The chloranilato ligands connect the Ln(III) ions and constitute the sides of the cavities. The dmso molecules point toward the rectangular cavities, precluding the inclusion of any crystallization solvent molecule. The rectangles are disposed with their long axis parallel, in a so-called brick-wall disposition (Figure 3a). The rectangular cavities are formed by four anilato whose rings are almost orthogonal to the average plane (*edge-on*, EO) and by two ligands with the anilato rings parallel to the average plane (*face-on*, *FO*, Figure 3b).

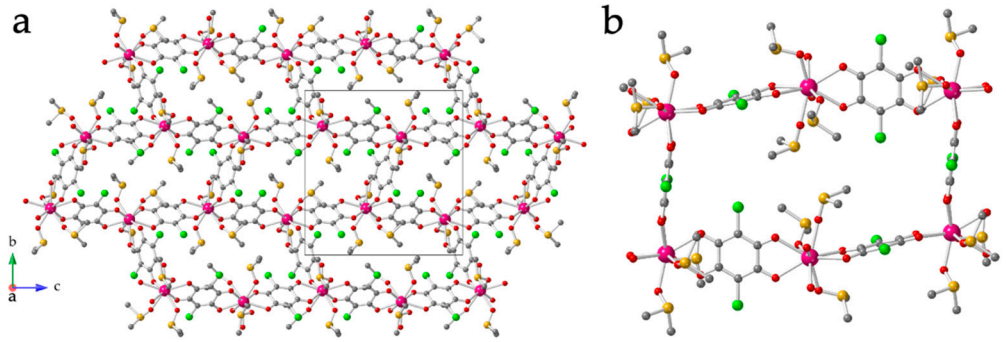


Figure 3. (**a**) View of one layer in compound **4** down the *a* direction. (**b**) View of one rectangular cavity in **4** down the direction perpendicular to the average ring plane. Colour code: C = grey, O = red, S = yellow, Cl = green and Nd = pink.

This structure is similar to the *c*-type structure defined by Robson [38,47], and is topologically equivalent to the (6,3) honeycomb layers found in other Ln-containing anilato-based compounds [25]. A clear proof of the large distortions of the hexagons and of the rectangular shape is provided by the values of the Ln–Ln distances along their three diagonals of the distorted hexagon (two long distances of ca. 20.5, 19.3 Å and a short one of ca. 10.7 Å; see below).

Although all the Ln(III) ions are equivalent, the spatial orientation of their coordination polyhedra is different, depending on the position of the Ln(III) ions in the rectangular cavities. Thus, the four Ln(III) ions located on the vertices of the rectangles have two dmso molecules pointing perpendicular to the plane of the rectangles, and the third one pointing towards the internal space of the cavity (Figure 3b). In contrast, the two Ln(III) ions located at the centre of the long sides of the rectangles present the opposite disposition (two dmso

molecules pointing towards the internal space of the cavity and one molecule perpendicular to the cavity plane).

3.3. Crystal Structure of [$Ln_2(C_6O_4Cl_2)_3(dmso)_4$]·2dmso·$2H_2O$ with Ln = Dy(**9**), *Ho*(**10**), *Er*(**11**), *Tm*(**12**) *and Yb*(**13**)

Compounds **9**–**13** are isostructural and crystallize in the triclinic *P*-1 space group. Note that the structure of compounds **9** and **11** has already been recently reported by us [32,37], and, therefore, we will only briefly describe it here to compare this phase II with phase I of compounds **1**–**8**.

Compounds **9**–**13** also show a (6,3)-gon honeycomb layered structure although with less distorted hexagons and much flatter layers. The coordination number (eight) and geometry (triangular dodecahedron, Table S8, supporting information) also change, due to the smaller size of the Ln(III) ions of this phase II (Dy–Yb).

3.4. Magnetic Properties of Compounds **1**–**13**

The magnetic properties of compounds **1**–**13** are displayed in Figure S1 (in Supplementary Materials). In all cases, the values of the product of the molar magnetic susceptibility times the temperature ($\chi_m T$) per formula (two Ln(III) ions) is within the expected range observed for many other isolated Ln(III) complexes and lattices (Table S9, supporting information). When the temperature is decreased, the $\chi_m T$ product shows a progressive decrease except in the Gd(III) sample. This progressive decrease is the expected one for magnetically isolated Ln(III) ions and can be attributed to the depopulation of the excited sublevels that appear due to the ligand field [48]. The magnetic isolation of the Ln(III) ions is similar to that found in other compounds with Ln(III) ions connected through bis-bidentate anilato ligands [28–33,37].

The good magnetic isolation provided by the chloranilato ligand, prompted us to measure the AC susceptibility to search for slow relaxation of the magnetization at low temperatures. Since the complete magnetic characterization of the Dy(III) compound (**9**) has recently been published by us [37], we have only measured the Tb (**8**), Ho (**10**) and Er (**11**) derivatives. These measurements show that compounds **8** and **10** do not present any slow relaxation of the magnetization at low temperatures neither with nor without an applied magnetic DC field. In contrast, the Er(III) derivative (**11**) shows a slow relaxation of the magnetization when a DC field is applied (Field-induced single-molecule magnet behaviour), although no χ''_m signal is observed for DC fields = 0 mT, probably due to the presence of a fast quantum tunnelling process for H_{DC} = 0 mT. Thus, at 1.9 K, compound **11** shows a frequency-dependent out of phase signal with a maximum at around 3000 Hz for DC fields > 0 mT. As the DC field increases, the maximum shifts to lower frequencies and its intensity increases to reach the maximum intensity at ca. 100 mT (Figure 4a).

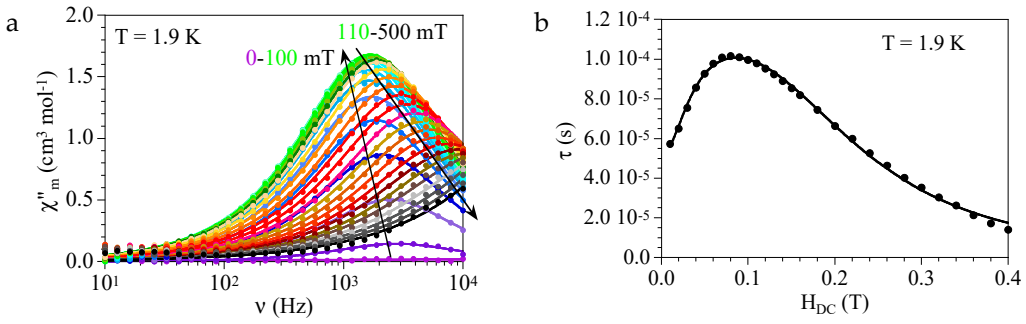


Figure 4. (**a**) Frequency dependence of the χ''_m signal at 1.9 K with different DC magnetic fields for compound **11**. Solid lines are the best fit to the Debye model. (**b**) Field dependence of the relaxation times of compound **11** at 1.9 K. Solid line if the best fit to Equation (2).

The fit of the frequency dependence to the Debye model (Equation (1), solid lines in Figure 4a) yields relaxation times (τ) that, as expected, show an initial increase when the DC field increases from 0 to ca. 100 mT and a decrease for higher DC values (Figure 4b).

$$\chi''(\omega) = \chi_S + \frac{(\chi_T - \chi_S)(\omega\tau)^{1-\alpha}\cos 1/2\alpha\pi}{1 + 2(\omega\tau)^{1-\alpha}\text{sen}1/2\alpha\pi + (\omega\tau)^{2(1-\alpha)}} \quad (1)$$

This field dependence of the relaxation time (τ) can be fit to a general model (Equation (2)), where H is the applied DC magnetic field, A corresponds to the quantum tunnelling mechanism (QTM), B_1 and B_2 to the Direct mechanism, D to the two field-independent mechanisms (Raman and Orbach) and n = 4 or 2 for Krammers and non-Kramers ions, respectively [49]. This equation reproduces very satisfactorily the field dependence of the relaxation times (τ), with the following parameters: A = 7.3(8) × 10^5 s^{-1} T^{-n}, n = 3.96(9), B_1 = 1.07(6) × 10^4 s^{-1}, B_2 = 1.6(2) × 10^3 T^{-2} and D = 8.6(2) × 10^3 s^{-1} (solid line in Figure 4b).

$$\tau^{-1} = AH^n + \frac{B_1}{1 + B_2H^2} + D \quad (2)$$

In order to determine the magnetic relaxation mechanisms with different applied DC fields, we have performed AC measurements at different temperatures and frequencies with applied DC fields of 20, 50 and 100 mT. These measurements show very similar frequency-dependent χ'_m (Figures S2–S4) and χ''_m signals (Figures S5 and S6 and Figure 5a) with an inflexion point in the χ'_m plot and a maximum in the χ''_m plot that shifts to higher frequencies as the temperature increases. Both signals can be fitted to the Debye model (solid lines in Figures S2–S6 and Figure 5a).

Table 1. Magnetic parameters in compound **11** for H_{DC} = 20, 50 and 100 mT.

H_{DC} (mT)	A (K^{-1})	τ_0 (s)	U_{eff} (K)
20	7.8(3) × 10^3	2(1) × 10^{-8}	21(2)
50	5.9(1) × 10^3	1.1(3) × 10^{-8}	23(1)
100	4.9(1) × 10^3	0.9(2) × 10^{-8}	24(1)

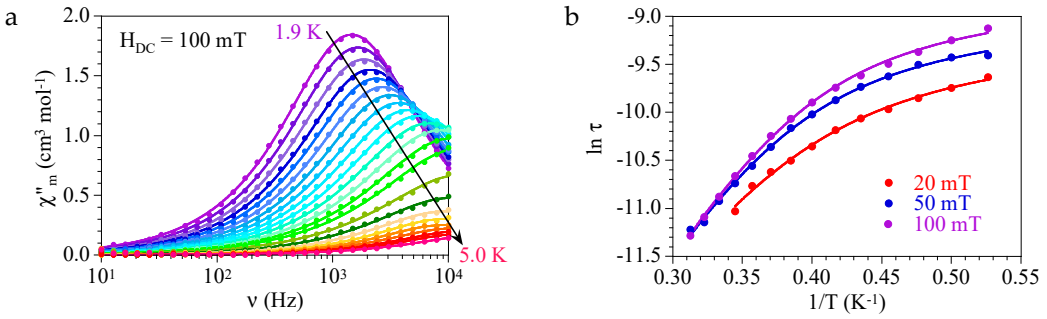


Figure 5. (**a**) Frequency dependence of χ''_m for compound **11** with H_{DC} = 100 mT in the temperature range 1.9–5.0 K. Solid lines are the best fit to the Debye model. (**b**) Arrhenius plot of the relaxation times for compound **11** with H_{DC} = 20, 50 and 100 mT. Solid lines are the best fit to the general model (Equation (3)) with Direct and Orbach contributions (see text and Table 1).

The Arrhenius plots (Figure 5b) of the relaxation times (τ) obtained in compound **11** with the Debye model (Equation (1)) for the three different DC fields, show a slight curvature, suggesting the presence of different mechanisms for the relaxation of the magnetization at low temperatures. If we assume that the quantum tunnelling has been completely suppressed by the application of a magnetic DC field, we can reproduce the thermal variation of the relaxation times using the general model, including a direct

(D, first term), Raman (R, second term) and Orbach (O, third term) mechanisms, as shown in Equation (3) [50].

$$\tau^{-1} = AT + CT^{n} + \tau_0^{-1} \exp\left(\frac{-U_{eff}}{T}\right) \quad (3)$$

Accordingly, we have fitted the relaxation times for H_{DC} = 20, 50 and 100 mT to the above equation. This fit shows that the Raman term is negligible and, therefore, we have used only the Direct and Orbach terms (solid lines in Figure 5b). This model reproduces the Arrhenius plot very well for the three different applied DC fields, with the parameters displayed in Table 1. As can be seen, the activation energies (in the range 21–24 K) are equal within experimental error and are similar to those observed in other anilato-based 2D lattices with slow relaxation of the magnetization as: $[Dy_{0.04}Eu_{1.96}(C_6O_4Br_2)_3(dmso)_6]\cdot 2dmso$ (40.9 K) [34], $[Dy_2(C_6O_4Br_2)_3(H_2O)_6]\cdot 8H_2O$ (9.6 K) [35], $[Dy_2(C_6O_4H_2)_3(dmso)_2(H_2O)_2]\cdot 2dmso\cdot 18H_2O$ (17.1 K) [37], $[Dy_2(C_6O_4Br_2)_3(dmf)_6]$ (11.4 and 36 K) [35], $[Dy_2(C_6O_4Cl_2)_3(dmso)_4]\cdot 2dmso\cdot 2H_2O$ (31.5 K) [37], $[Dy_2(C_6O_4Br_2)_3(dmso)_4]\cdot 2dmso\cdot 2H_2O$ (22.8 K) [37] and $[Dy_2(C_6O_4(CN)Cl_2)_3(dmso)_6]$ (21 K) [37]. As can be seen in the previous list, compound **11** is the first Er(III) anilato-based lattice showing slow relaxation of the magnetization.

4. Discussion

It is interesting to note that compounds **1**–**13** have been synthesized using the same solvent, stoichiometry, concentrations and ligand, but changing only the precursor Ln(III) nitrate salt. Therefore, the structural differences have to be attributed to the Ln(III) ion. As already mentioned, the complete series La–Yb crystallize in two different phases (I and II) formulated as $[Ln_2(C_6O_4Cl_2)_3(dmso)_6]$ with Ln = La(**1**), Ce(**2**), Pr(**3**), Nd(**4**), Sm(**5**), Eu(**6**), Gd(**7**) and Tb(**8**) (Phase I) or $[Ln_2(C_6O_4Cl_2)_3(dmso)_4]\cdot 2dmso\cdot 2H_2O$ with Ln = Dy(**9**), Ho(**10**), Er(**11**), Tm(**12**) and Yb(**13**) (Phase II). Both phases are 2D lattices with a 6,3-gon structure, but there are important differences in: (a) the coordination number and geometry, (b) the distortions of the rings, (c) the planarity of the layers, (d) the presence of crystallization solvent molecules and (e) the packing mode of the layers. As we will see below, all these differences derive from the different coordination number and geometry, a direct consequence of the size of the Ln(III) ion.

The first clear difference is the coordination number and geometry: capped square antiprism for the larger ions: La–Tb, (Figure 6b), in phase I (Table S7, supporting information) and triangular dodecahedron for the smaller ions Dy–Yb (Figure 6c), in phase II (Table S8, supporting information). The continuous size reduction of the Ln(III) ions along the series can be clearly seen in the Ln–O bond distances (Tables S10 and S11). As can be seen in Figure 6a, the average Ln–O bond distances with the anilato ligands and with the dmso molecules linearly decrease as we move along the lanthanoid series and show an abrupt change when passing from Tb to Dy, corresponding to the change in the coordination number and geometry. The average Ln–O bond distances with the chloranilato ligand ($Ln–O_{anilato}$) are longer than the average Ln–O bond distances with the dmso molecules ($Ln–O_{dmso}$). The longer $Ln–O_{anilato}$ distances can be attributed to the tension of the bite angle in the chelating chloranilato ligand that precludes a shortening of the Ln–O bond distances. In contrast, the dmso molecules are monodentate and can get closer to the Ln(III). From Dy(III) to Yb(III), the ions are too small to accept the nonacoordination and, accordingly, are octacoordinated. As expected, the reduction in the coordination number leads to an abrupt reduction of the average Ln–O bond distances when passing from Tb(III) to Dy(III) (Figure 6a).

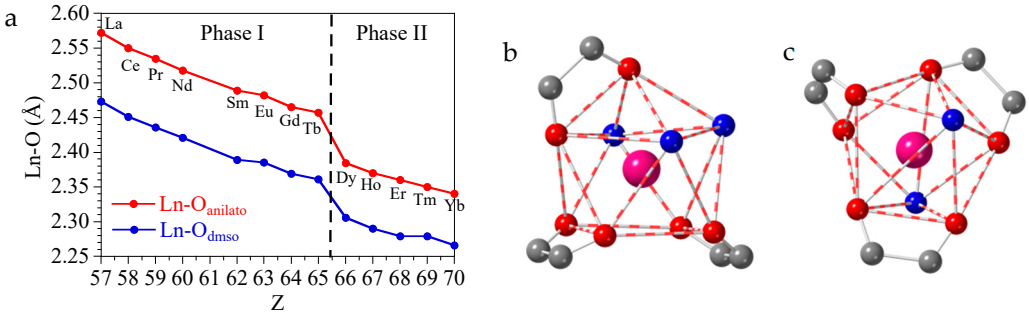


Figure 6. (**a**) Variation of the average Ln–$O_{anilato}$ and Ln–O_{dmso} bond distances along the series of compounds **1**–**13**. Coordination geometries in compounds (**b**) **1**–**8** and (**c**) **9**–**13**. Colour code: Ln = pink, $O_{anilato}$ = red, O_{dmso} = blue and C = grey.

Besides the coordination geometry, the change in the coordination number leads to a change in the symmetry of the lattice, which passes from a monoclinic $P2_1/n$ space group in phase I (compounds **1**–**8**) to a triclinic P-1 space group in phase II (compounds **9**–**13**). This change reflects the different spatial dispositions of the three chloranilato ligands in both phases (Figure 6b,c). The different orientation of the anilato bridges leads to the above indicated disposition of the anilato rings with respect to the plane of the ring in phase I (four anilato rings of the type *edge-on*, EO and two *face-on, FO*, Figure 3b). In contrast, in phase II, the disposition of the anilato rings in the opposite: four FO and two EO [32,37]. Although both phases present the same 6,3-gon topology, the different spatial orientations of the chloranilato ligands lead to differences in two important structural features: (i) the geometry of the 6-membered rings (distorted rectangles, in phase I, Figure 7a, vs. distorted hexagons in phase II, Figure 7b) and (ii) the planarity of the layers (very corrugated layers in phase I, Figure 7c, but almost flat layers in phase II, Figure 7d).

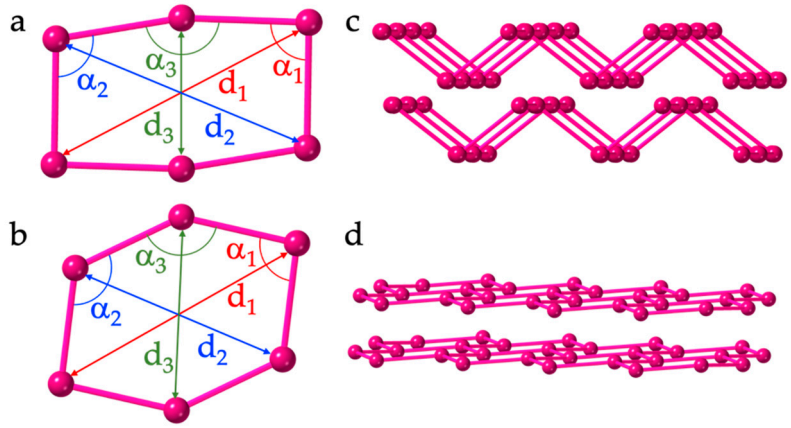


Figure 7. Top view of the six-membered rings in phase I (**a**) and II (**b**) indicating the three different diagonals and Ln–Ln–Ln angles. Side view of the layers in phase I (**c**) and II (**d**). Only the Ln(III) ions are displayed for clarity and the pink lines represent the chloranilato bridges.

The distortions in the six-membered rings can clearly be observed in the Ln–Ln distances along the three diagonals of the hexagons (d_1, d_2 and d_3, Figure 7) and in the three Ln–Ln–Ln angles inside the ring (α_1, α_2 and α_3, Figure 7). These distances and angles (Table S12, supporting information) change abruptly when passing from Tb to Dy along the series (Figure 8). To quantify these distortions, we have calculated the sum of the deviations of the three diagonals from the average value ($\Sigma \mid d_i - d_{av} \mid$, Table S12, supporting information) and the sum of the deviations from 120° of the three Ln–Ln–Ln angles inside the ring ($\Sigma \mid \alpha_i - 120 \mid$, Table S12, supporting information).

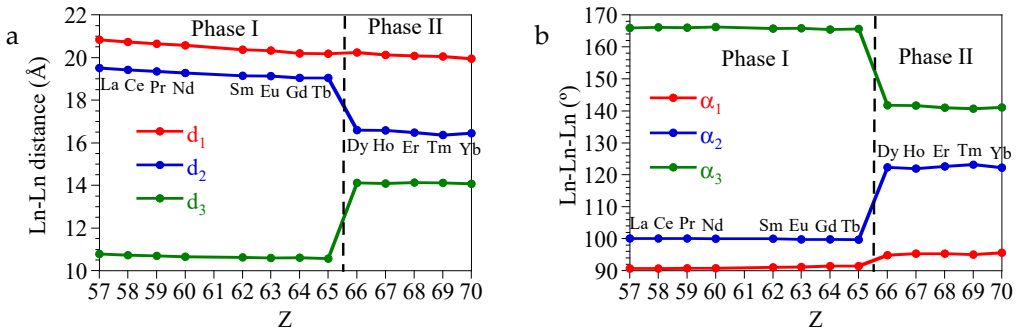


Figure 8. Variation of the Ln–Ln distances along the three diagonals (**a**) and the three internal Ln–Ln–Ln angles (**b**) in the hexagonal rings in compounds **1**–**13**. The definitions of d_i and α_i are shown in Figure 7.

As can be seen in Figure 9a, both values show a slight decrease as we move forward in the lanthanoids series, due to the decrease in the ionic radii. As expected, both values are much higher in phase I (La–Tb) than in phase II (Dy–Yb), confirming the much important deviations from the regular hexagon for the rings in phase I. An additional effect of the decrease in the ionic radii along the Ln(III) series is the reduction of the SHAPE parameters for both coordination geometries (Figure 9b).

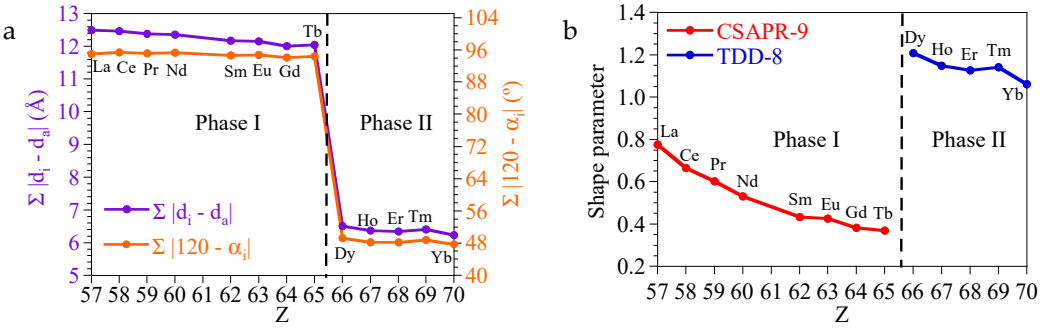


Figure 9. (**a**) Variation of $\Sigma\,|\,d_i - d_{av}\,|$ (purple dots, left scale) and $\Sigma\,|\,120 - \alpha_i\,|$ (orange dots, right scale) in compounds **1**–**13**. (**b**) Variation of the SHAPE parameter for the coordination environment of the Ln(III) ions in compounds **1**–**13** (CSAPR-9 = capped square antiprism; TDD-8 = triangular dodecahedron).

A final difference that can be found between both phases is the presence of two dmso and two water molecules in the hexagonal cavities in phase II. In contrast, in phase I there are no crystallization solvent molecules, probably due to the lack of free space inside the rectangular cavities.

5. Conclusions

We have synthesized and structurally characterized the complete series of anilato-based 2D lattices formulated as $[Ln_2(C_6O_4Cl_2)_3(dmso)_6]$ with Ln = La (**1**), Ce (**2**), Pr (**3**), Nd (**4**), Sm (**5**), Eu (**6**), Gd (**7**) and Tb (**8**) (phase I) or $[Ln_2(C_6O_4Cl_2)_3(dmso)_4]\cdot 2dmso\cdot 2H_2O$ with Ln = Dy (**9**), Ho (**10**), Er (**11**), Tm (**12**) and Yb (**13**) (phase II). This study has shown that the size of the Ln(III) ion determines the coordination number and geometry of the Ln(III) ion and, therefore, the final structure of the compounds. Thus, the largest Ln(III) ions (La–Tb, phase I) have a coordination number of nine and a geometry of capped square antiprism, whereas the smallest ions (Dy–Yb, phase II) show a coordination number of eight and a geometry of triangular dodecahedron. Although both phases are 2D lattices with 6,3-gon topology, the different coordination numbers and geometry lead to important structural differences in both phases: (i) The six-membered rings are distorted rectangles in phase I and distorted hexagons in phase II. (ii) The layers in phase I are very corrugated, but are

almost flat in phase II, (iii) There are two dmso and two water molecules in the distorted hexagonal cavities in phase II, but no solvent molecules in the rectangular cavities in phase I.

The magnetic properties show that the Er derivative behaves as a field-induced single-molecule magnet at low temperatures and that the magnetization relaxes following Direct and Orbach mechanisms with an activation energy of 21–24 K for applied DC fields in the range 20–100 mT.

Supplementary Materials: The following supporting information can be downloaded at: https://www.mdpi.com/article/10.3390/cryst12020261/s1, Figure S1. Thermal variation of the $\chi_m T$ product per formula unit (two Ln(III) ions) for compounds **1**–**13**. Figure S2. Frequency dependence of χ'_m for compound **11** with H_{dc} = 20 mT in the temperature range 1.9–5.0 K. Figure S3. Frequency dependence of χ'_m for compound **11** with H_{dc} = 50 mT in the temperature range 1.9–5.0 K. Figure S4. Frequency dependence of χ'_m for compound **11** with H_{dc} = 100 mT in the temperature range 1.9–5.0 K. Figure S5. Frequency dependence of χ''_m for compound **11** with H_{dc} = 20 mT in the temperature range 1.9–5.0 K. Figure S6. Frequency dependence of χ''_m for compound **11** with H_{dc} = 50 mT in the temperature range 1.9–5.0 K; Table S1. Crystal size and colour, exact amounts and precursors used for the synthesis of compounds **1**–**13**. Table S2. Crystal data and structure refinement parameters for compounds $[Ln_2(C_6O_4Cl_2)_3(dmso)_6]$ with Ln = La(**1**), Ce(**2**) and Pr(**3**). Table S3. Crystal data and structure refinement parameters for compounds $[Ln_2(C_6O_4Cl_2)_3(dmso)_6]$ with Ln = Nd(**4**), Sm(**5**) and Eu(**6**). Table S4. Crystal data and structure refinement parameters for compounds $[Ln_2(C_6O_4Cl_2)_3(dmso)_6]$ with Ln = Gd(**7**) and Tb(**8**). Table S5. Crystal data and structure refinement parameters for compounds $[Ln_2(C_6O_4Cl_2)_3(dmso)_4]\cdot 2dmso\cdot 2H_2O$ with Ln = Dy(**9**), Ho (**10**) and Er(**11**). Table S6. Crystal data and structure refinement parameters for compounds $[Ln_2(C_6O_4Cl_2)_3(dmso)_4]\cdot 2dmso\cdot 2H_2O$ with Ln = Tm(**12**) and Yb(**13**). Table S7. Continuous SHAPE measurement (CShM) values of the 13 possible coordination geometries for the Ln(III) ion with coordination number nine in compounds **1**–**8**. Table S8. Continuous SHAPE measurement (CShM) values of the 13 possible coordination geometries for the Ln(III) ion with coordination number eight in compounds **9**–**13**. Table S9. Experimental and calculated room temperature $\chi_m T$ values for compounds **1**–**13**. Table S10. Ln–O bond distances (in Å) in compounds **1**–**8**. Table S11. Ln–O bond distances (in Å) in compounds **9**–**13**. Table S12. Ln–Ln distances (Å) along the three diagonals and Ln–Ln–Ln angles (°) in the hexagonal rings in **1**–**13**.

Author Contributions: Conceptualization, S.B. and C.J.G.-G.; Data curation, S.B., C.J.G.-G. and A.H.-P.; Formal analysis, S.B. and C.J.G.-G.; Funding acquisition, C.J.G.-G.; Investigation, S.B., C.J.G.-G. and A.H.-P.; Methodology, S.B., C.J.G.-G. and A.H.-P.; Project administration, C.J.G.-G.; Supervision, S.B. and C.J.G.-G.; Writing—original draft, C.J.G.-G.; Writing-review & editing, S.B., C.J.G.-G. and A.H.-P. All authors have read and agreed to the published version of the manuscript.

Funding: We thank the grant CTQ2017-87201-P funded by MCIN/AEI/10.13039/501100011033 and by "ERDF A way of making Europe" for financial support and the Generalidad Valenciana (Prometeo/2019/076). A.H.P. thanks the Grant FPU17/03216 funded by MCIN/AEI/10.13039/501100011033 and by "ESF Investing in your future".

Data Availability Statement: The data presented in this study are available on request from the corresponding author.

Conflicts of Interest: The authors declare no conflict of interest. The funders had no role in the design of the study; in the collection, analyses, or interpretation of data; in the writing of the manuscript, or in the decision to publish the results.

References

1. Batten, S.R.; Champness, N.R.; Chen, X.; Garcia-Martinez, J.; Kitagawa, S.; Öhrström, L.; O'Keeffe, M.; Suh, M.P.; Reedijk, J. Terminology of metal–organic Frameworks and Coordination Polymers (IUPAC Recommendations 2013). *Pure Appl. Chem.* **2013**, *85*, 1715–1724. [CrossRef]
2. Zhang, X.; Chen, Z.; Liu, X.; Hanna, S.L.; Wang, X.; Taheri-Ledari, R.; Maleki, A.; Li, P.; Farha, O.K. A Historical Overview of the Activation and Porosity of metal–organic Frameworks. *Chem. Soc. Rev.* **2020**, *49*, 7406–7427. [CrossRef] [PubMed]
3. Zhou, H.C.; Long, J.R.; Yaghi, O.M. Introduction to Metal-Organic Frameworks. *Chem. Rev.* **2012**, *112*, 673–674. [CrossRef] [PubMed]

4. Furukawa, H.; Cordova, K.E.; O'Keeffe, M.; Yaghi, O.M. The Chemistry and Applications of Metal-Organic Frameworks. *Science* **2013**, *341*, 1230444. [CrossRef] [PubMed]
5. Shu-Na, Z.; Wang, G.; Poelman, D.; Van Der Voort, P. Metal Organic Frameworks Based Materials for Heterogeneous Photocatalysis. *Molecules* **2018**, *23*, 2947.
6. Zhao, X.; Wang, Y.; Li, D.; Bu, X.; Feng, P. Metal–Organic Frameworks for Separation. *Adv. Mater.* **2018**, *30*, 1705189. [CrossRef]
7. Canivet, J.; Fateeva, A.; Guo, Y.; Coasne, B.; Farrusseng, D. Water Adsorption in MOFs: Fundamentals and Applications. *Chem. Soc. Rev.* **2014**, *43*, 5594–5617. [CrossRef]
8. Li, H.; Zhao, S.; Zang, S.; Li, J. Functional metal–organic Frameworks as Effective Sensors of Gases and Volatile Compounds. *Chem. Soc. Rev.* **2020**, *49*, 6364–6401. [CrossRef]
9. Kreno, L.E.; Leong, K.; Farha, O.K.; Allendorf, M.; Van Duyne, R.P.; Hupp, J.T. Metal-Organic Framework Materials as Chemical Sensors. *Chem. Rev.* **2012**, *112*, 1105–1125. [CrossRef]
10. Campbell, M.G.; Dinca, M. Metal-Organic Frameworks as Active Materials in Electronic Sensor Devices. *Sensors* **2017**, *17*, 1108. [CrossRef]
11. Xie, L.S.; Skorupskii, G.; Dincă, M. Electrically Conductive Metal–Organic Frameworks. *Chem. Rev.* **2020**, *120*, 8536–8580. [CrossRef] [PubMed]
12. Lim, D.; Kitagawa, H. Rational Strategies for Proton-Conductive metal–organic Frameworks. *Chem. Soc. Rev.* **2021**, *50*, 6349–6368. [CrossRef] [PubMed]
13. Asadi, K.; van der Veen, M.A. Ferroelectricity in Metal–Organic Frameworks: Characterization and Mechanisms. *Eur. J. Inorg. Chem.* **2016**, *2016*, 4332–4344. [CrossRef]
14. Kurmoo, M. Magnetic Metal-Organic Frameworks. *Chem. Soc. Rev.* **2009**, *38*, 1353–1379. [CrossRef] [PubMed]
15. Li, B.; Wen, H.M.; Cui, Y.; Zhou, W.; Qian, G.; Chen, B. Emerging Multifunctional Metal-Organic Framework Materials. *Adv. Mater.* **2016**, *28*, 8819–8860. [CrossRef] [PubMed]
16. Chakraborty, G.; Park, I.; Medishetty, R.; Vittal, J.J. Two-Dimensional Metal-Organic Framework Materials: Synthesis, Structures, Properties and Applications. *Chem. Rev.* **2021**, *121*, 3751–3891. [CrossRef]
17. Wang, M.; Dong, R.; Feng, X. Two-Dimensional Conjugated metal–organic Frameworks (2D c-MOFs): Chemistry and Function for MOFtronics. *Chem. Soc. Rev.* **2021**, *50*, 2764–2793. [CrossRef]
18. Benmansour, S.; Vallés-García, C.; Gómez-Claramunt, P.; Mínguez Espallargas, G.; Gómez-García, C.J. 2D and 3D Anilato-Based Heterometallic M(I)M(III) Lattices: The Missing Link. *Inorg. Chem.* **2015**, *54*, 5410–5418. [CrossRef]
19. Atzori, M.; Artizzu, F.; Sessini, E.; Marchio, L.; Loche, D.; Serpe, A.; Deplano, P.; Concas, G.; Pop, F.; Avarvari, N.; et al. Halogen-Bonding in a New Family of Tris(Haloanilato)Metallate(Iii) Magnetic Molecular Building Blocks. *Dalton Trans.* **2014**, *43*, 7006–7019. [CrossRef]
20. Benmansour, S.; Gómez-Claramunt, P.; Vallés-García, C.; Mínguez Espallargas, G.; Gómez García, C.J. Key Role of the Cation in the Crystallization of Chiral Tris(Anilato)Metalate Magnetic Anions. *Cryst. Growth Des.* **2016**, *16*, 518–526. [CrossRef]
21. Kitagawa, S.; Kawata, S. Coordination Compounds of 1,4-Dihydroxybenzoquinone and its Homologues. Structures and Properties. *Coord. Chem. Rev.* **2002**, *224*, 11–34. [CrossRef]
22. Abrahams, B.F.; Grannas, M.J.; Hudson, T.A.; Hughes, S.A.; Pranoto, N.H.; Robson, R. Synthesis, Structure and Host-Guest Properties of $(Et_4N)_2[Sn^{IV}Ca^{II}(Chloranilate)_4]$, a New Type of Robust Microporous Coordination Polymer with a 2D Square Grid Structure. *Dalton Trans.* **2011**, *40*, 12242–12247. [CrossRef] [PubMed]
23. Benmansour, S.; Gómez-García, C.J. A Heterobimetallic Anionic 3,6-Connected 2D Coordination Polymer Based on Nitranilate as Ligand. *Polymers* **2016**, *8*, 89. [CrossRef] [PubMed]
24. Mercuri, M.L.; Congiu, F.; Concas, G.; Sahadevan, S.A. Recent Advances on Anilato-Based Molecular Materials with Magnetic and/or Conducting Properties. *Magnetochemistry* **2017**, *3*, 17. [CrossRef]
25. Benmansour, S.; Gómez-García, C.J. Lanthanoid-Anilato Complexes and Lattices. *Magnetochemistry* **2020**, *6*, 71. [CrossRef]
26. Atzori, M.; Benmansour, S.; Mínguez Espallargas, G.; Clemente-León, M.; Abhervé, A.; Gómez-Claramunt, P.; Coronado, E.; Artizzu, F.; Sessini, E.; Deplano, P.; et al. A Family of Layered Chiral Porous Magnets Exhibiting Tunable Ordering Temperatures. *Inorg. Chem.* **2013**, *52*, 10031–10040. [CrossRef]
27. Benmansour, S.; Gómez-García, C.J. Heterometallic Anilato-Based Layered Magnets. *Gen. Chem.* **2020**, *6*, 190033. [CrossRef]
28. Benmansour, S.; López-Martínez, G.; Canet-Ferrer, J.; Gómez-García, C.J. A Family of Lanthanoid Dimers with Nitroanilato Bridges. *Magnetochemistry* **2016**, *2*, 32. [CrossRef]
29. Benmansour, S.; Pérez-Herráez, I.; López-Martínez, G.; Gómez García, C.J. Solvent-Modulated Structures in Anilato-Based 2D Coordination Polymers. *Polyhedron* **2017**, *135*, 17–25. [CrossRef]
30. Gómez-Claramunt, P.; Benmansour, S.; Hernández-Paredes, A.; Cerezo-Navarrete, C.; Rodríguez-Fernández, C.; Canet-Ferrer, J.; Cantarero, A.; Gómez-García, C.J. Tuning the Structure and Properties of Lanthanoid Coordination Polymers with an Asymmetric Anilato Ligand. *Magnetochemistry* **2018**, *4*, 6. [CrossRef]
31. Benmansour, S.; Hernández-Paredes, A.; Gómez-García, C.J. Effect of the Lanthanoid-Size on the Structure of a Series of Lanthanoid-Anilato 2-D Lattices. *J. Coord. Chem.* **2018**, *71*, 845–863. [CrossRef]
32. Benmansour, S.; Pérez-Herráez, I.; Cerezo-Navarrete, C.; López-Martínez, G.; Martínez Hernandez, C.; Gómez-García, C.J. Solvent-Modulation of the Structure and Dimensionality in Lanthanoid-Anilato Coordination Polymers. *Dalton Trans.* **2018**, *47*, 6729–6741. [CrossRef] [PubMed]

33. Benmansour, S.; Hernández-Paredes, A.; Gómez-García, C.J. Two-Dimensional Magnetic Coordination Polymers Formed by Lanthanoids and Chlorocyananilato. *Magnetochemistry* **2018**, *4*, 58. [CrossRef]
34. Hernández-Paredes, A.; Cerezo-Navarrete, C.; Gómez García, C.J.; Benmansour, S. Slow Relaxation in Doped Coordination Polymers and Dimers Based on Lanthanoids and Anilato Ligands. *Polyhedron* **2019**, *170*, 476–485. [CrossRef]
35. Benmansour, S.; Hernández-Paredes, A.; Mondal, A.; López Martínez, G.; Canet-Ferrer, J.; Konar, S.; Gómez-García, C.J. Slow Relaxation of the Magnetization, Reversible Solvent Exchange and Luminescence in 2D Anilato-Based Frameworks. *Chem. Commun.* **2020**, *56*, 9862–9865. [CrossRef]
36. Mondal, A.; Roy, S.; Konar, S. Remarkable Energy Barrier for Magnetization Reversal in 3D and 2D Dysprosium-Chloranilate-Based Coordination Polymers. *Chem. Eur. J.* **2020**, *26*, 8774–8783. [CrossRef]
37. Benmansour, S.; Hernández-Paredes, A.; Bayona-Andrés, M.; Gómez-García, C.J. Slow Relaxation of the Magnetization in Anilato-Based Dy(III) 2D Lattices. *Molecules* **2021**, *26*, 1190. [CrossRef]
38. Abrahams, B.F.; Coleiro, J.; Ha, K.; Hoskins, B.F.; Orchard, S.D.; Robson, R. Dihydroxybenzoquinone and Chloranilic Acid Derivatives of Rare Earth Metals. *J. Chem. Soc. Dalton Trans.* **2002**, 1586–1594. [CrossRef]
39. Diaz-Torres, R.; Alvarez, S. Coordinating Ability of Anions and Solvents Towards Transition Metals and Lanthanides. *Dalton Trans.* **2011**, *40*, 10742–10750. [CrossRef]
40. Alvarez, S. Coordinating Ability of Anions, Solvents, Amino Acids, and Gases towards Alkaline and Alkaline-Earth Elements, Transition Metals, and Lanthanides. *Chem. Eur. J.* **2020**, *26*, 8663. [CrossRef]
41. Bain, G.A.; Berry, J.F. Diamagnetic Corrections and Pascal's Constants. *J. Chem. Educ.* **2008**, *85*, 532–536. [CrossRef]
42. Oxford Diffraction Crysalispro. 2004. 171.33.55. Available online: https://www.rigaku.com/products/crystallography/crysalis (accessed on 10 February 2022).
43. Altomare, A.; Burla, M.C.; Camalli, M.; Cascarano, G.L.; Giacovazzo, C.; Guagliardi, A.; Moliterni, A.G.G.; Polidori, G.; Spagna, R. SIR97: A New Tool for Crystal Structure Determination and Refinement. *J. Appl. Cryst.* **1999**, *32*, 115–119. [CrossRef]
44. Sheldrick, G.M. Crystal Structure Refinement with SHELXL. *Acta Cryst. C* **2015**, *71*, 3–8. [CrossRef]
45. Farrugia, L.J. WinGX and ORTEP for Windows: An Update. *J. Appl. Cryst.* **2012**, *45*, 849–854. [CrossRef]
46. Álvarez, S. Distortion Pathways of Transition Metal Coordination Polyhedra Induced by Chelating Topology. *Chem. Rev.* **2015**, *115*, 13447–13483. [CrossRef] [PubMed]
47. Riley, P.E.; Haddad, S.F.; Raymond, K.N. Preparation of Praseodymium(III) Chloranilate and the Crystal Structures of $Pr_2(C_6Cl_2O_4)_3 \cdot 8C_2H_5OH$ and $Na_3[C_6H_2O(OH)(SO_3)_2] \cdot H_2O$. *Inorg. Chem.* **1983**, *22*, 3090–3096. [CrossRef]
48. Sorace, L.; Gatteschi, D. *Electronic Structure and Magnetic Properties of Lanthanide Molecular Complexes*; Layfield, R.A., Murugesu, M., Eds.; Wiley-VCH Verlag GmbH & Co.: Weinheim, Germany, 2015; Volume 1, pp. 1–25.
49. Dey, A.; Kalita, P.; Chandrasekhar, V. Lanthanide(III)-Based Single-Ion Magnets. *ACS Omega* **2018**, *3*, 9462–9475. [CrossRef] [PubMed]
50. Demir, S.; Zadrozny, J.M.; Long, J.R. Large Spin-Relaxation Barriers for the Low-Symmetry Organolanthanide Complexes Cp*2Ln(BPh4)] (Cp*=pentamethylcyclopentadienyl; Ln=Tb, Dy). *Chem. Eur. J.* **2014**, *20*, 9524–9529. [CrossRef]